

Template-Synthesized Nanoscopic Gold Particles: Optical Spectra and the Effects of Particle Size and Shape

Colby A. Foss, Jr.,[†] Gabor L. Hornyak, Jon A. Stockert, and Charles R. Martin*

Department of Chemistry, Colorado State University, Fort Collins, Colorado 80523

Received: August 30, 1993; In Final Form: January 3, 1994*

We have prepared nanoscopic gold cylinders of controlled radius and aspect ratio via electrodeposition of the metal within the pores of anodically-grown porous aluminum oxide membranes. The nanocylinder radii are determined by the pore dimensions of the host alumina which, in turn, depend on anodization conditions. The particle aspect ratios were controlled by varying the amount of Au deposited within the pores. The optical spectra of the gold nanocylinder/alumina composites exhibit strong absorption bands in the visible spectrum. The extinction maxima (λ_{\max}) values for gold particles approaching spherelike geometry agree well with Mie theory calculations. The blue shift of λ_{\max} as the particle aspect ratio is increased is in qualitative agreement with Maxwell-Garnett theory. We propose a simple modification of Maxwell-Garnett theory that addresses both size and shape effects.

I. Introduction

The optical properties of nanoscopic metal particles have attracted and still attract a great deal of interest.^{1a–c} Indeed, it has been almost a century since Gustav Mie demonstrated how particle size gives rise to the various colors of colloidal gold solutions.^{2a,b} In more recent times, attention has focused on the application of such small metal particles in surface-enhanced spectroscopy,^{3a,b} photocatalysis,^{4a,b} colored anodizing,⁵ and selective solar absorbers.^{6a,b}

Most work to date on the optical properties of nanoscopic metal particles has involved methods that preclude control of particle shape and orientation with respect to the electric field of the incident light. Exceptions to this include the work of Liao and co-workers who prepared ordered arrays of ellipsoidal silver particles with aspect ratios as high as 3:1 using photolithography.⁷ In our laboratories we have developed methods based on the template synthesis strategy in which various materials are deposited within the pores of host membranes such as track-etched polycarbonate⁸ and anodic aluminum oxide.^{9a,b} The microstructure of the host material and other conditions of deposition thus define particle geometry and orientation.

In our efforts to understand the optical properties of submicrometer metallic particles, we have found that anodic aluminum oxides are ideal host templates: they are optically transparent over a wide range ($0.3 \mu\text{m} \leq \lambda \leq 6 \mu\text{m}$) and the parallel alignment of the cylindrical pores means that the template-synthesized metal particles are also aligned in one direction. Hence, the particles can be studied without removing the host template, and there is no ambiguity in particle orientation.

In our early work we relied upon commercially available anodic aluminas,^{9a,b} which contain pores *ca.* $0.25 \mu\text{m}$ in diameter. In these membranes, we prepared cylindrical gold particles with aspect ratios (defined as the particle length, A , divided by its diameter, B) as high as 10:1. The resulting Au/Al₂O₃ composites showed significant transparency in the infrared spectrum but not at shorter wavelengths where $0.25 \mu\text{m}$ diameter particles scattered appreciably.

In a recent note, we presented preliminary results of our optical characterization of gold cylinders template-synthesized in anodic alumina membranes prepared in our laboratory.¹⁰ The mem-

TABLE 1: Experimental Results: Gold Nanoparticle Dimensions

anodic voltage (V)	no. C Au(I) ^a (C)	particle radius ^b (nm)	particle length ^b (nm)	aspect ratio ^c (A/B)	κ^d
40	0.20	30 ± 3	92 ± 12	1.53	1.65
40	0.40	30 ± 3	132 ± 6	2.20	1.46
40	0.70	30 ± 3	268 ± 16	4.47	1.22
40	1.00	30 ± 3	434 ± 22	7.23	1.14
50	0.20	38 ± 2	98 ± 8	1.29	1.78
50	0.40	38 ± 2	160 ± 6	2.11	1.48
50	0.70	38 ± 2	256 ± 7	3.37	1.30
50	1.00	38 ± 2	406 ± 7	5.34	1.19
70	0.20	43 ± 2	130 ± 20	1.51	1.67
70	0.40	43 ± 2	192 ± 20	2.23	1.45
70	0.70	43 ± 2	360 ± 40	4.14	1.24
70	1.00	43 ± 2	390 ± 70	4.51	1.22
90	0.20	60 ± 5	120 ± 50	1.02	1.98
90	0.40	60 ± 5	410 ± 30	3.38	1.29
90	0.70	60 ± 5	640 ± 100	5.28	1.18
90	1.00	60 ± 5	800 ± 200	6.31	1.16

^a Number of coulombs of Au(I) reduced over the electrode area.

^b Determined from transmission electron microscopy. ^c Defined as the particle length, A , divided by the particle diameter, B . In the text, $A = 2a$ and $B = 2b$. ^d M-G screening parameter (see text).

branes prepared in that study had much smaller pores (*ca.* 50 nm in diameter), and the resulting particles showed extinction maxima in the visible spectrum reminiscent of aqueous gold colloids of similar size. In that work, we demonstrated how the template synthesis approach allows for simple control of gold nanocylinder aspect ratio and that varying the particle aspect ratio gives rise to systematic shifts in the extinction maximum.¹⁰ We also showed that the observed effects of particle shape are qualitatively consistent with the predictions of Maxwell-Garnett theory (M-G), which is a simple treatment for composite materials that addresses particle shape and orientation but not size.^{11b}

In this paper, we present the results of a study in which we have systematically varied both nanocylinder aspect ratio and diameter. We show how the template synthesis method is a convenient means by which one can control these parameters and hence the composite's optical properties. Because there is no ambiguity in nanocylinder orientation with respect to the incident field, the analysis of size and shape effects on optical spectra should be greatly simplified. We compare the spectra of the gold nanocylinder/alumina composites with the predictions of M-G theory and Mie scattering theory.^{2b} We also propose an approximation

* Corresponding author.

[†] Current address: Department of Chemistry, Georgetown University, Washington, D.C. 20057.

• Abstract published in *Advance ACS Abstracts*, February 15, 1994.

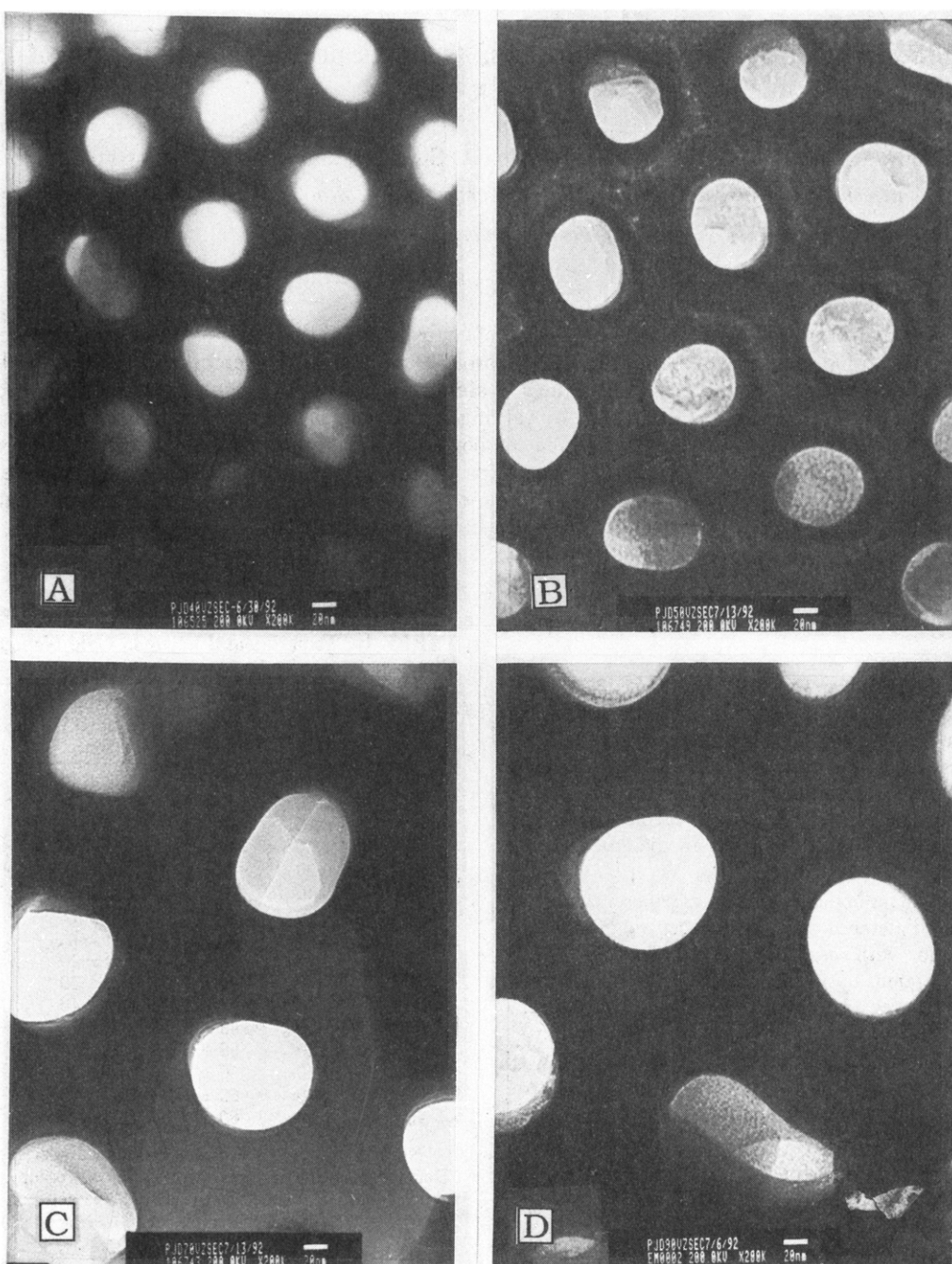


Figure 1. Transmission electron micrographs of facial (*z*-section) micrometeor sections of gold plated anodic alumina membranes grown under the conditions: (A) 40 V in 4% oxalic acid; (B) 50 V in 4% oxalic acid; (C) 70 V in 2% oxalic acid; (D) 90 V in 2% oxalic acid. Scale bar in each case is 20 nm. Note: gold nanoparticles are not visible in these sections.

within the M-G framework that addresses both the size and shape of the nanoscopic particles.

II. Theory: Mie Scattering and Maxwell-Garnett Treatments for Nanoscopic Particles

In this section, we review two approaches that we use to model the optical spectra of composites containing nanoscopic particles. Mie scattering theory is a rigorous formulation for particles of any size but is limited to spherical geometry and interparticle separation distances which are much larger than the wavelength of the incident light.^{2a,b} Maxwell-Garnett (M-G) theory is strictly valid only in the limit where particle dimensions and separation distances are infinitely small relative to the wavelength but can be easily generalized to particles of various shapes.^{11b} In our experiments, because we vary both size and shape of the gold particles, each of these approaches has something to offer in the interpretation of the optical spectra.

In the Mie approach, the total transmittance through a film containing spherical metal particles is given by^{2b}

$$T_{\text{tot}} = \exp(-N\pi a^2 Q_{\text{ext}} d) \quad (1)$$

where N is the number concentration of spheres per unit volume, a is the sphere radius, and d is the film thickness. The extinction coefficient Q_{ext} is related to the Mie scattering coefficients a_n and b_n through^{2b}

$$Q_{\text{ext}} = \left(\frac{2}{x^2} \right) \sum_{n=1}^{\infty} (2n+1) \operatorname{Re}(a_n + b_n) \quad (2)$$

where $x = 2\pi a n_0 / \lambda$ (n_0 is the refractive index of the host medium and λ is the wavelength of the incident light *in vacuo*). The term Re in eq 2 signifies the real part of the complex function in parentheses. The scattering coefficients a_n and b_n describe the

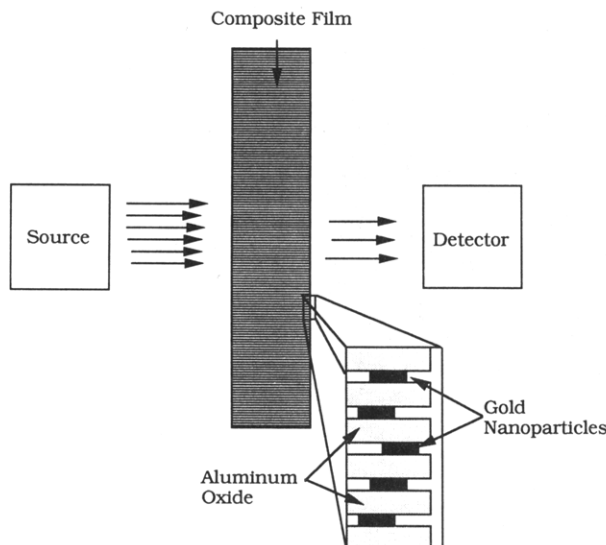


Figure 2. Schematic of optical transmission experiment for gold/alumina composites. The cylindrical particles are aligned with their principal axes (A) parallel to the direction of light incidence.

amplitudes of the scattered electric and magnetic fields, respectively^{2b}, and are given by

$$a_n = \frac{\psi'_n(y)\psi_n(x) - m\psi_n(y)\psi'_n(x)}{\psi'_n(y)\xi_n(x) - m\psi_n(y)\xi'_n(x)} \quad (3a)$$

$$b_n = \frac{m\psi'_n(y)\psi_n(x) - \psi_n(y)\psi'_n(x)}{m\psi'_n(y)\xi_n(x) - \psi_n(y)\xi'_n(x)} \quad (3b)$$

where m is related to the complex refractive index of the metal, \tilde{n}_m , and to the host medium refractive index, n_0 , via

$$m = \tilde{n}_m/n_0 \quad (4a)$$

$$\tilde{n}_m = n_m + ik_m \quad (4b)$$

where n_m is the real refractive index of the metal and k_m is the absorption coefficient. The quantity y in eqs 3a and 3b is equal to $2\pi a \tilde{n}_m / \lambda$. The primes in eqs 3a and 3b signify first derivatives with respect to the argument.

The functions ψ_n and ξ_n are related to the Bessel (J_n) and second-order Hankel (H_n^2) functions via^{2b,12}

$$\psi_n(z) = (z\pi/2)^{1/2} J_{n+1/2}(z) \quad (5a)$$

$$\xi_n(z) = (z\pi/2)^{1/2} H_{n+1/2}^{(2)}(z) \quad (5b)$$

where z is equal to x or y .

For metal particles less than ca. 100 nm in diameter, the Mie scattering treatment for visible wavelengths requires only the first two or three expansion terms in eq 2. Nonetheless, the computation is still quite tedious. A quite different approach which is valid when the metal particle dimensions are much smaller than the wavelength of light was developed by Maxwell-Garnett.^{11a} M-G theory assumes that it is reasonable to define an effective complex dielectric constant $\tilde{\epsilon}_c$ for a composite containing metal particles (with complex dielectric constant $\tilde{\epsilon}_m$) embedded in a host matrix (with complex dielectric constant ϵ_0) through

$$\left(\frac{\tilde{\epsilon}_c - \tilde{\epsilon}_0}{\tilde{\epsilon}_c + 2\tilde{\epsilon}_0} \right) = f_m \left(\frac{\tilde{\epsilon}_m - \tilde{\epsilon}_0}{\tilde{\epsilon}_m + 2\tilde{\epsilon}_0} \right) \quad (6)$$

where f_m is the volume fraction of metal in the composite. The complex dielectric constant is related to the optical refractive

index n and absorption coefficient k via

$$\tilde{\epsilon} = \tilde{n}^2 = \epsilon' + i\epsilon'' \quad (7a)$$

$$\epsilon' = n^2 - k^2 \quad (7b)$$

$$\epsilon'' = 2nk \quad (7c)$$

where ϵ' is the real part of the dielectric constant and ϵ'' is the imaginary component (the refractive index n is not to be confused with the summation index in eqs 2 and 3).

Maxwell-Garnett's original work addressed spherical inclusions, and it is for this specific geometry that the factor 2 appears in the denominators of eq 6. This factor is also called the screening parameter^{11b} and is in general denoted κ . Hence, while $\kappa = 2$ for spheres, long needlelike particles oriented with their axes of revolution parallel to the direction of light incidence have a κ value that approaches unity. On the other hand, κ approaches infinity for thin flat disks oriented with their axes of revolution perpendicular to the light incidence.

From a knowledge of ϵ_m , ϵ_0 , f_m , and κ , one can derive the effective dielectric constant ϵ_c for the composite, and then, via eq 7a-c, the effective composite optical constants n_c and k_c can be calculated. The total transmittance is then given by¹³

$$T_{\text{tot}} = \left[1 - \frac{(n_c - 1)^2 + k_c^2}{(n_c + 1)^2 + k_c^2} \right]^2 \exp(-4\pi k_c d/\lambda) \quad (8)$$

where d is the film thickness and λ is the incident wavelength. The term preceding the exponential accounts for reflective losses at the film/air interface.¹⁴

III. Experimental Section

A. Porous Alumina Membrane Preparation. Nanoporous alumina template membranes were prepared by anodization of aluminum (Aldrich 2-mm plate, 99.99% purity) in aqueous oxalic acid media. Anodization of aluminum to yield porous oxides is a well-established technique and has been discussed extensively in the literature.^{15a-c} For details on how the porous oxide is removed from the aluminum substrate, consult ref 16.

Our two-electrode anodization cell consisted of an insulated thermostat-controlled plastic bucket (ca. 19 L), a 6 cm × 10 cm stainless steel cathode and a 10 cm × 10 cm Al plate anode. Voltage control was provided by a Sorensen DCR-9B power supply.

Pore diameters in anodic aluminas are roughly proportional to the applied voltage in potential-controlled anodization.¹⁶ In this study, we prepared membranes with pores of four different diameters. Anodization at 40 and 50 V in 4% (w/v) oxalic acid yielded membranes with pore diameters of approximately 60 and 76 nm, respectively. Anodization at 70 and 90 V in 2% (w/v) oxalic acid produced pores with diameters of approximately 86 and 120 nm, respectively. The electrolyte temperature was maintained between 0 and 7 °C. Membranes were grown from 30 to 40 μm in thickness before removal. Figure 1 shows transmission electron micrographs (TEMs) of facial sections of alumina composite membranes prepared under the above conditions. The porosity of these membranes is in the range of 25–30%.

B. Gold Nanoparticle Preparation. Gold nanoparticles were prepared by electrodeposition of Au(I) (Technic Inc., Orotemp 24 gold plating solution) within the pores of the alumina membranes. The details of this procedure are given in ref 9b. Four levels of gold consisting of 0.20, 0.40, 0.70, and 1.00 C, were deposited in each of the four types of membranes. The membrane area of each sample was approximately 3.14 cm² (when considering the porosity, the actual electrode area varied between 0.78 and 0.94 cm²). The potentiostat employed was an EG&G

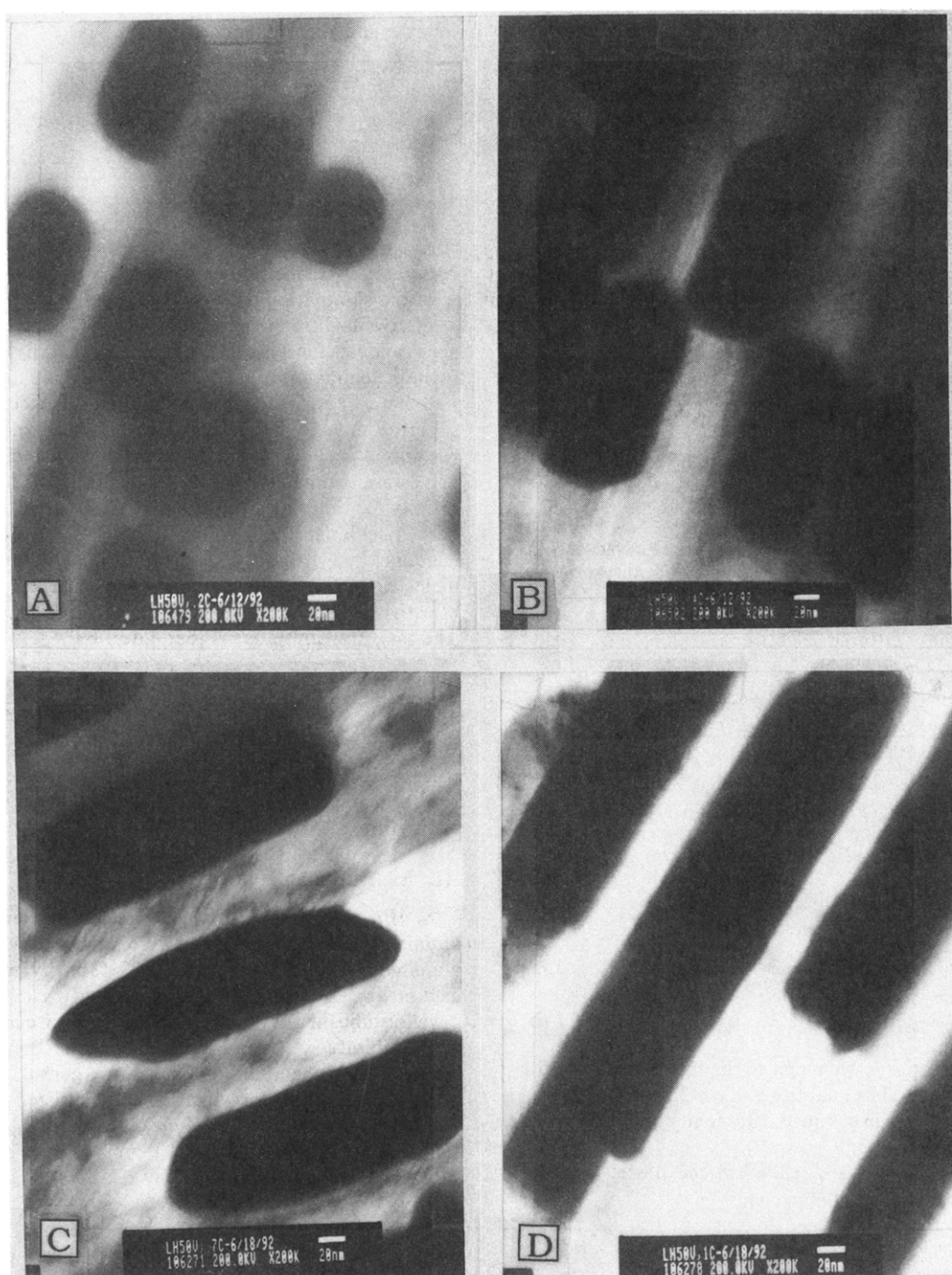


Figure 3. Transmission electron micrographs of gold particles prepared by electrodeposition of gold into oxalic acid membranes prepared under 50 V anodizing conditions. (A) 0.20C, (B) 0.40C, (C) 0.70C, and (D) 1.00C Scale bar in each case is 20 nm.

Princeton Applied Research Model 173 equipped with a Model 179 digital coulometer.

C. Anodic Alumina and Gold Nanoparticle/Alumina Composite Characterization. Alumina pore radii and gold nanoparticle dimensions were determined by means of transmission electron microscopy (JEOL 2000 TEM). The thin sample sections required for these analyses were obtained by diamond-knife microtome. UV/visible/near-IR spectra were obtained using a Hitachi U-3501 spectrometer. Figure 2 shows a schematic of the experimental optical configuration used to examine the gold nanocylinder/alumina composites.

IV. Results

The template syntheses method allows for straightforward control of nanocylinder size, shape, and orientation. Figure 3 shows TEM images of cross sections of alumina membranes (prepared at 50 V in 4% oxalic acid) after the deposition of Au

into the pores. At low deposition levels like 0.20 C, the particles are short and spherelike. At higher deposition levels such as 1.00 C, the particles become longer and needlelike within the cylindrical radius held constant by the pore walls. Table 1 summarizes the results of measurements of particle dimensions for the various pore radius/gold deposition combinations as obtained from TEM images. Although it is apparent that a distribution of sizes and shapes exists within a sample composite film, the qualitative dependence of λ_{\max} on size and shape correlates very well with the average values of experimentally derived particle aspect ratios and radii.

The TEM images of the gold/alumina composites also show that the gold particles do not lie at a uniform distance from the membrane face but rather through a layer *ca.* 1 μm in thickness. We discussed the reasons for this in a previous paper and also how this nonuniform particle placement affects the optical path

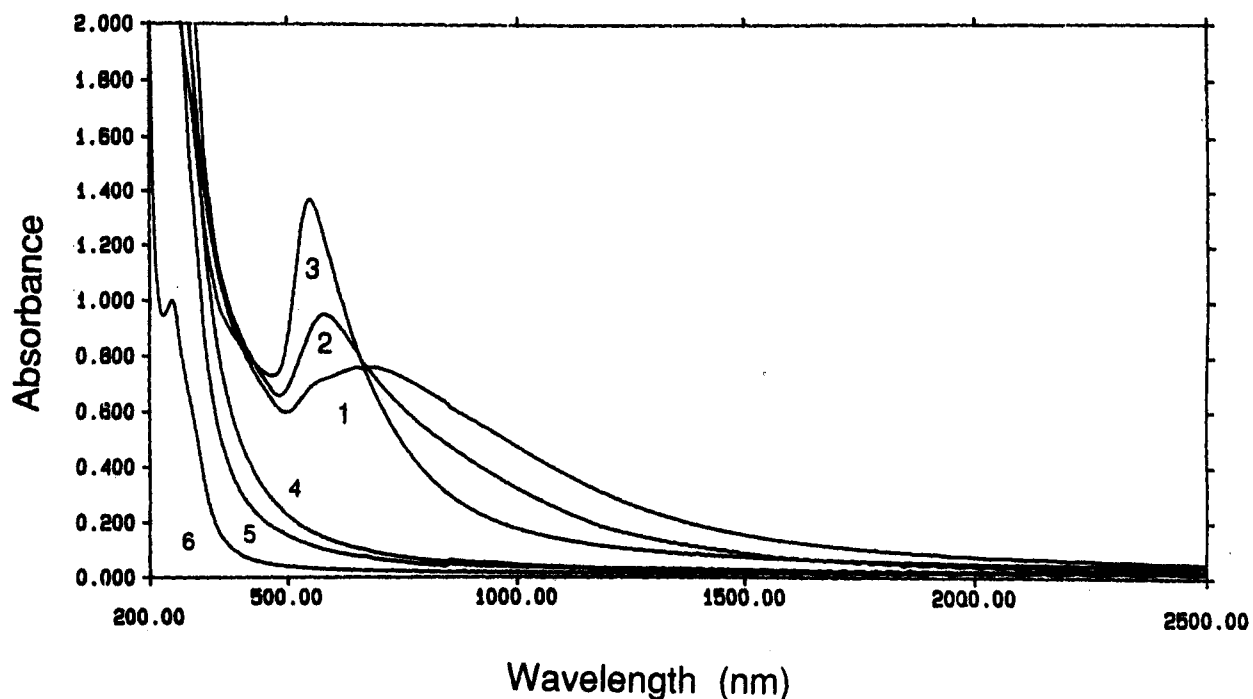


Figure 4. UV/vis/near-IR spectra for blank anodic alumina membranes and gold particle/alumina composites in which the particles are nearly spherical. Curve 1, particle radius 60 nm; curve 2, particle radius 43 nm; curve 3, particle radius 30 nm; curve 4, blank 30 nm pore radius alumina; curve 5, blank 43 nm pore radius alumina; curve 6, blank 60 nm pore radius alumina.

length, d , and metal volume fraction, f_m .^{9b} We will discuss this point further in the next section.

Figure 4 shows UV/vis/near-IR extinction spectra¹⁷ for three composites of different pore radii in which the gold nanoparticles are short and nearly spherical (curves 1, 2, and 3). In each case the composite exhibits a significant transparency in the near-IR region of the spectrum and a strong extinction band in the visible. The wavelength of maximum extinction increases with increasing particle radius giving rise to color variations in the different gold particles radius composites. The transmitted light for the 30 nm radius particles appears red-purple while 60 nm radius particles appear blue-green. This trend is consistent with the colors exhibited by colloidal gold particles of different sizes in aqueous solutions.^{2b} The 60 nm radius particle composite also shows a weak shoulder (*ca.* 550 nm) on the broad band centered at 655 nm.

The dependence of the optical spectra on particle shape is shown in Figure 5. As the aspect ratio increases, the extinction intensity increases and λ_{\max} shifts to shorter wavelengths. This trend is seen for all composite systems considered in this study and is summarized in Figure 6, where λ_{\max} is plotted against the natural logarithm of the aspect ratio, $\ln(A/B)$. The two smaller pore radius systems (30 and 38 nm) show λ_{\max} values that converge at high aspect ratios. The larger pore systems exhibit similar trends with respect to shape, but the λ_{\max} values are red-shifted relative to the small particle radius composites.

Thus there are two trends immediately apparent for gold nanocylinder particles aligned with their principal axes parallel to the direction of light incidence. First of all, λ_{\max} red-shifts with increasing cylinder radius for particles of all aspect ratios (Figure 6). Second, for constant cylinder radius, λ_{\max} blue-shifts as the particle aspect ratio is increased (Figure 6).

V. Discussion

A. Comparison of Spectra of Spherelike Gold Particles with Mie Calculations. As was mentioned in the previous section, deposition of small amounts of gold gives rise to particles whose aspect ratios are nearly unity. It is of interest then to compare the experimental spectra for these spherical particle composites with spectra calculated using Mie theory. The calculation requires

a knowledge of the particle radii (which we obtain from the TEM measurements), the values of the optical constants for the metal particles and host membrane for the spectral range of interest, and finally the particle density N and optical path length d . The values of n_m and k_m for gold were taken from ref 18. For the host medium, we assumed $n_0 = 1.6$.¹⁹ While the anodic aluminas used in this study are slightly absorbing in the visible spectrum ($k_0 < 10^{-3}$), we assumed $k_0 = 0$ to avoid complex arguments in the parameter x of eqs 3a and 3b and thus simplify the calculation.

We computed Q_{ext} using eqs 2–4 with $n = 1–3$. We have found that the third term in eq 2 is negligible for all particle sizes considered in this study. The total transmittance was then calculated from eq 1, with particle density N and composite path length d chosen so as to yield extinction intensities comparable to experiment (*vide infra*).

The Mie-calculated spectra shown in Figure 7 are in good qualitative agreement with the experimental spectra. As the sphere radius increases, the extinction maximum shifts to longer wavelengths and decreases in intensity. The calculated spectra also exhibit increased band broadening with particle size, though not to the extent seen in experiment (see Figure 4). In addition, we have examined by means of Mie theory simulations the effect of size distribution for spheres on spectral broadening but find that distributions consistent with TEM images cannot account for the degree of broadening exhibited in the experimental spectra.

As shown in Figure 6, the lowest aspect ratio particles are still somewhat prolate (*i.e.*, their aspect ratios are greater than unity). Hence, in order to compare the experimental and Mie theory λ_{\max} values, we extrapolated the experimental λ_{\max} values shown in Figure 6 to unit aspect ratio using a quadratic fit of λ_{\max} versus $\ln(A/B)$. Table 2 summarizes these λ_{\max} values extrapolated from experiment as well as those calculated from Mie theory. It is evident that the quantitative agreement is quite satisfactory.

The Mie-calculated spectrum for the 60 nm radius particles exhibits a shoulder at 530 nm which compares favorably with the weak shoulder seen in the experimental spectrum at *ca.* 550 nm. In the Mie treatment, this band is due to the gold sphere quadrupole mode and arises from the $n = 2$ index term in eq 2 and 3.²⁰ This mode is negligible in all but the 60 nm radius

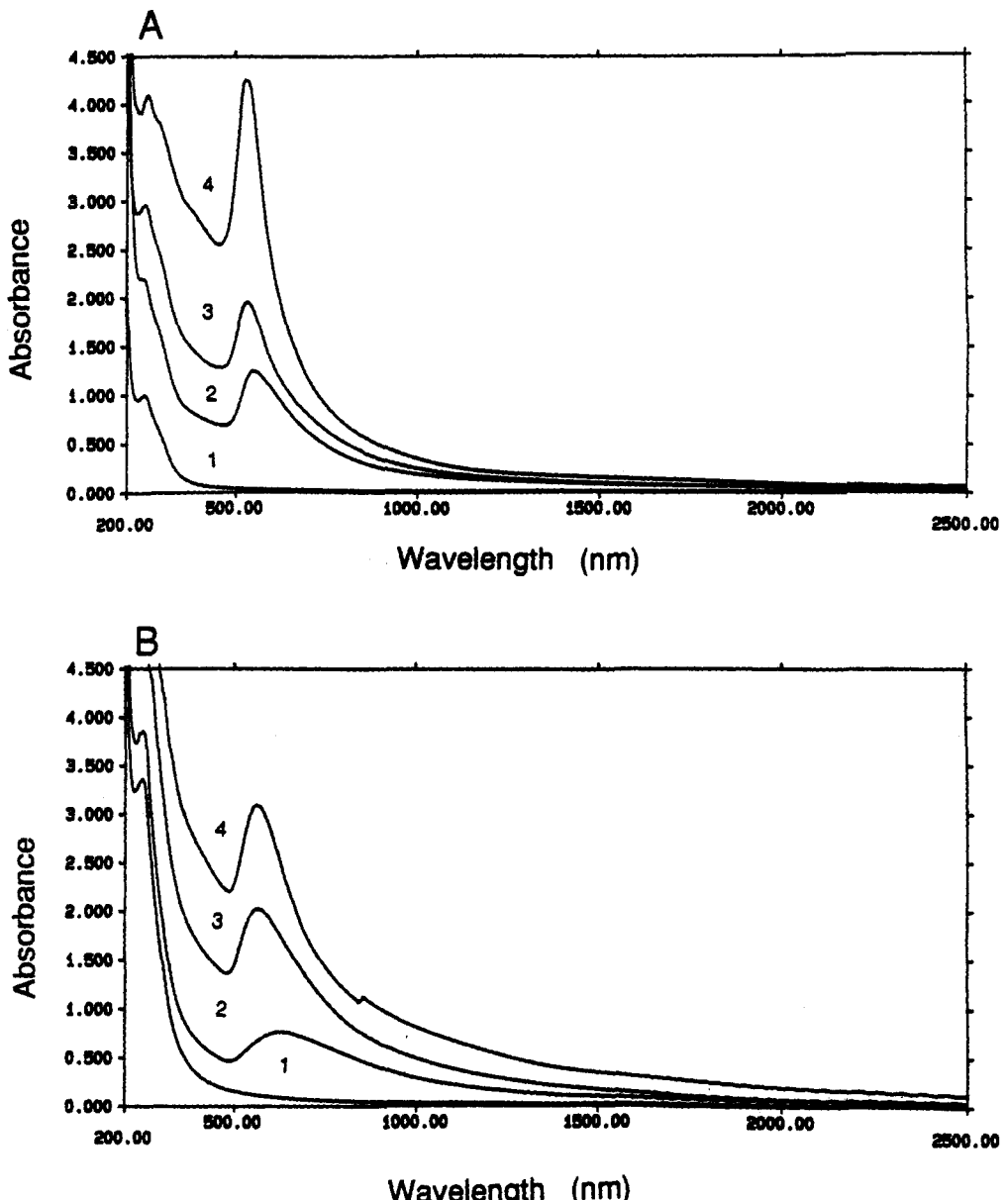


Figure 5. UV/vis/near-IR spectra for gold particle/alumina composites containing particles of various aspect ratios. Particle length in all cases equals $2a$, where a is the magnitude of the semimajor axis. (A) 30 nm pore radius systems: curve 1, blank membrane (*ca.* 30 μm in thickness) prepared at 40 V in 4% oxalic acid; curve 2, $2a = 92$ nm; curve 3, $2a = 132$ nm; curve 4, $2a = 268$ nm. (B) 60 nm pore radius membranes prepared at 90 V in 2% oxalic acid: curve 1, blank alumina membrane; curve 2, $2a = 120$ nm; curve 3, $2a = 410$ nm; curve 4, $2a = 800$ nm.

calculation. For the particle radius range considered in this study, the leading dipole term ($n = 1$) predominates.

In principle, it should be possible to determine the particular concentration N using

$$N = 3f_m/4\pi a^3 \quad (9)$$

As we discussed in a previous paper, because of the geometry of the oxide pores and the manner in which the particles are created in the pores, the metal volume fraction should be related to the intrinsic porosity P of the host membrane and the optical path length d via^{9b}

$$f_m = P(2a/d) \quad (10)$$

In fact, when we attempted spectral calculations using N based on eqs 9 and 10, with estimates of P and d from TEM images, the extinction intensities were much higher than those seen experimentally (the λ_{\max} results are not affected by N in the Mie treatment). Although the reasons for this apparent discrepancy are not explicitly known, the values of the experimental and

simulated spectra converge if lower porosities are input into the Mie calculations.

B. Particle Shape Effects in the Maxwell-Garnett Limit. If a composite contains particles whose dimensions are much smaller than the wavelength of the incident light, then the Maxwell-Garnett formulation of eq 6 is applicable. Because eq 6 does not address particle size, it cannot be used to model size effects on extinction maxima as in the case of Mie theory. On the other hand, particle shape determines the screening parameter κ , and hence will be manifest in the composite optical properties n_c and k_c .

In our attempts to model shape effects in the experimental spectra, we treat the gold nanocylinders as ellipsoids of revolution. The long axis, A , of the particle is thus identified with twice the semimajor axis a of an ellipsoid. The semiminor axis b is then the particle's cylindrical radius where $2b = B$, the short axis or diameter of the particle.

The M-G screening parameter κ is related to the Lorentz depolarization factor q through^{11b}

$$\kappa = (1/q) - 1 \quad (11)$$

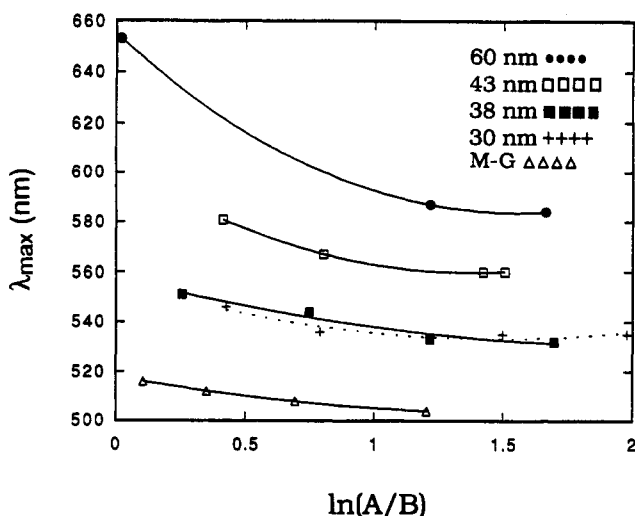


Figure 6. Summary of λ_{\max} dependence on particle shape. The experimentally derived cylindrical radii are given in the figure legend ($b = 60, 43, 38$, and 30 nm, where b is the magnitude of the semiminor axis or cylindrical radius). The values for the aspect ratio (A/B) are taken from Table 1. The theoretical M-G calculation yields the λ_{\max} values shown in the curve labeled M-G. The lines between the data points were derived from statistical best fit curves.

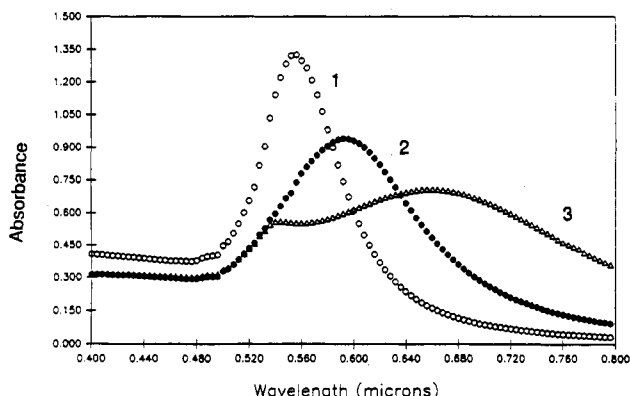


Figure 7. Spectra calculated from Mie theory (eqs 1–3). Input parameters as follows: curve 1, radius $a = 30$ nm, particle density $N = 57.5 \mu\text{m}^{-3}$; curve 2, $a = 43$ nm, $N = 19.5 \mu\text{m}^{-3}$; curve 3, $a = 60$ nm, $N = 9.95 \mu\text{m}^{-3}$. The optical path length is $1 \mu\text{m}$ in all cases. Host medium $n_0 = 1.6$.

TABLE 2: Comparison of λ_{\max} Values from Experiment, Mie Theory, and the Dynamical M-G Model (λ_{\max} in nm) for Spherical Particles

particle radius (nm) ^a	exptal values ^b	Mie theory calcn	dynamical M-G model calcn
30	556	556	568
38	559	576	608
43	604	592	636
60	656	658	756

^a Determined from transmission electron microscopy. ^b Extrapolated values from experimental data shown in Figure 6 (see text).

The factor q depends on the shape of the particle. For an electric field incident along the long axis A of a prolate ellipsoid, the depolarization factor q_a is given by^{2b}

$$q_a = \frac{1 - \zeta^2}{\zeta^2} \left[\frac{1}{2\zeta} \ln \left(\frac{1 + \zeta}{1 - \zeta} \right) - 1 \right] \quad (12a)$$

where

$$\zeta = 1 - (b/a)^2 \quad (12b)$$

In our study, the gold particles are aligned with their principal axes parallel to the direction of light incidence. The electric field is thus incident along the short axes of the particles. For the

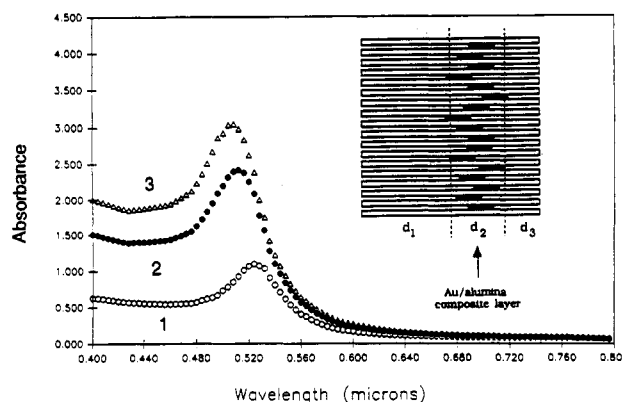


Figure 8. Absorption spectra calculated from simple M-G theory using eqs 6–8. (Inset: The three layer model assumed for calculations.) The input parameters are as follows: curve 1, $\kappa = 2, f_m = 0.0065, d_2 = 1 \mu\text{m}, d_1 = 28 \mu\text{m}$; curve 2, $\kappa = 1.4, f_m = 0.025, d_2 = 1.07 \mu\text{m}, d_1 = 27.93$; curve 3, $\kappa = 1.22, f_m = 0.034, d_2 = 1.21 \mu\text{m}, d_1 = 27.79 \mu\text{m}$. The d_3 layer equals $1 \mu\text{m}$ in all cases.

special case of an ellipsoid of revolution, we can relate the depolarization factor along the long axis (q_a) to q_b , the depolarization factor along the short axis via²¹

$$q_b = (1 - q_a)/2 \quad (13)$$

In our experiments, low amounts of deposited gold leads to particles that are nearly spherical. In the spherical limit (as $A/B \rightarrow 1$), the depolarization factor q_b is equal to $1/3$ and κ is equal to 2. However, as we increase the amount of gold deposited, the aspect ratio increases, and as it approaches infinity ($A/B \rightarrow \infty$). Eqs 11–13 lead to $q_b = 1/2$ and $\kappa = 1$. It is thus relevant to examine the M-G-calculated spectra for $1 < \kappa \leq 2$.

Figure 8 shows absorption spectra calculated using M-G theory for composites containing gold ellipsoids of varying aspect ratios such that $1 < \kappa \leq 2$. As in the case of the Mie calculations, the optical properties of gold were taken from ref 18. For the host oxide, we used complex f_0 values obtained in this laboratory.²² We modeled the experimental membranes as three-layer systems in which the gold/alumina composite layer is sandwiched between two layers of alumina which contain no gold (see inset of Figure 8). Thus there are four interfaces where reflective losses occur in addition to the absorption losses in the composite and alumina layers.^{9b}

The M-G-calculated spectra shown in Figure 8 agree qualitatively with experimental data (see Figure 5a,b). As the gold particle aspect ratio increases, the absorption intensity increases (due to the attendant increase in path length and metal volume fraction). However, the increase in aspect ratio also engenders a decrease in κ and λ_{\max} shifts to shorter wavelengths. This effect is seen in the experimental spectra for all pore diameter systems, as summarized in Figure 6. The lowest curve in Figure 6 describes the shape effect on λ_{\max} in the M-G limit. All experimental λ_{\max} values are shifted red relative to the M-G limit.

In the M-G limit, the dependence of λ_{\max} on particle shape can be understood in terms of the particle dipole resonance condition often discussed in the surface-enhanced Raman spectroscopy (SERS) literature.^{3b} The wavelength of highest absorption in the metal particle composite corresponds to the condition where the induced field in the metal is maximal. This occurs when the real component of the metal dielectric constant ϵ_m' is equal to $-\kappa\epsilon_0'$. Hence, the right-hand side of eq 6 becomes very large (assuming the imaginary component of the metal and host dielectric functions are very small and the composite dielectric function is maximized). The real dielectric constant ϵ_m' for gold (and most metals) is negative in sign and monotonically decreases at wavelengths above the plasma edge.²³ Hence, if κ decreases, the dipole resonance condition occurs at a shorter wavelength.

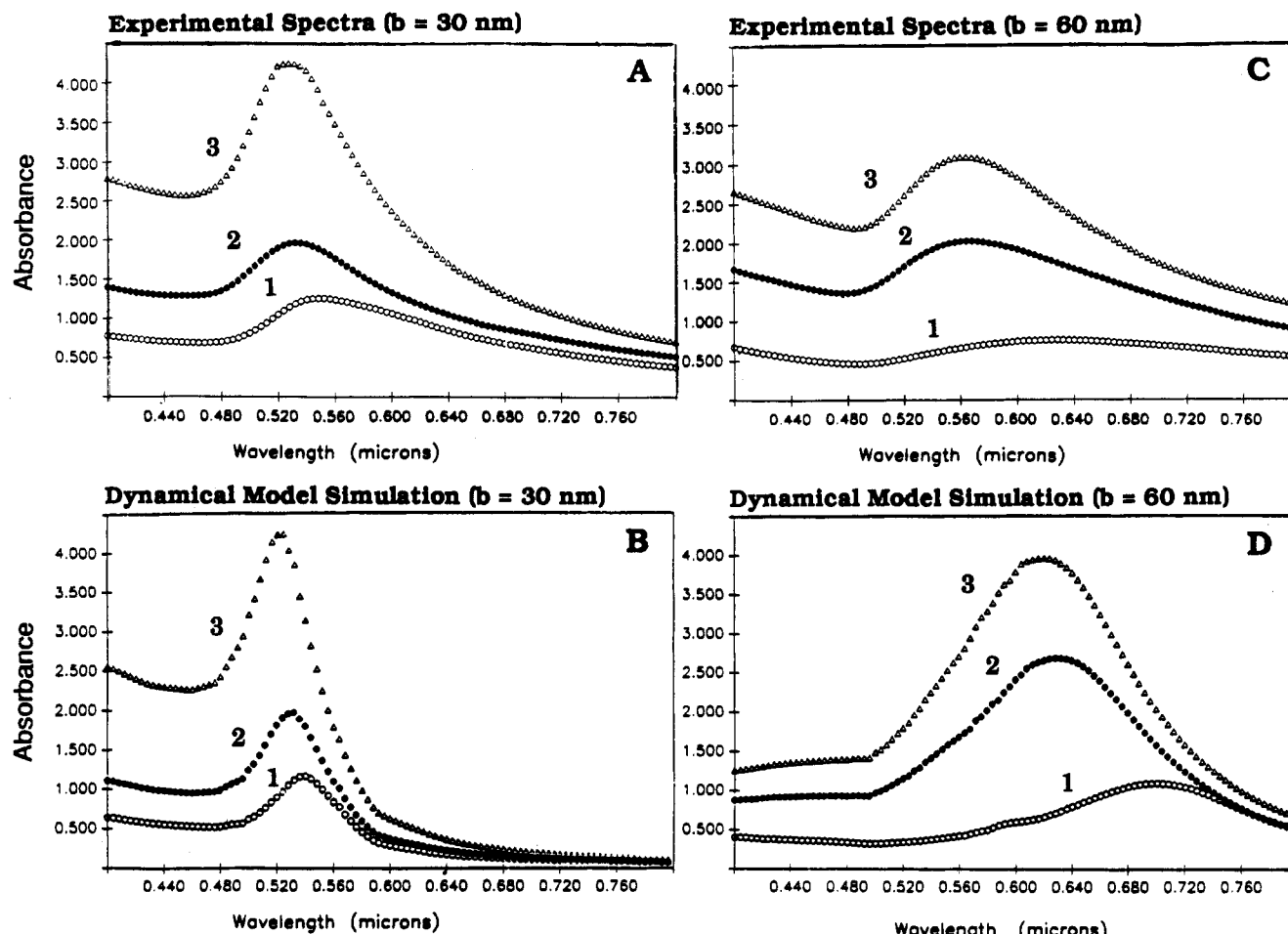


Figure 9. Absorption spectra calculated using M-G theory with size-adjusted depolarization factor q_{eff} . (A) Experimental spectrum for $b = 30$ nm radius particles in which the wavelength region between 0.400 and 0.800 μm of Figure 5A is shown for comparison. Curves 1, 2, and 3 correspond to spectra of $a = 46, 66$, and 134 nm, respectively. (B) Simulated spectra for $b = 30$ nm radius system-input parameters: curve 1, $a = 46$ nm, $f_m = 0.0065$, $d_2 = 1$ μm , $d_1 = 28$ μm ; curve 2, $a = 66$ nm, $f_m = 0.0133$, $d_2 = 1.070$ μm , $d_1 = 27.93$ μm ; curve 3, $a = 134$ nm, $f_m = 0.217$, $d_2 = 1.208$ μm , $d_1 = 27.79$ μm . (C) Experimental spectrum for $b = 60$ nm radius particles in which the wavelength region between 0.400 and 0.800 μm is shown for comparison. Curves 1, 2, and 3 correspond to spectra of $a = 60, 205$, and 320 nm, respectively. (D) Simulated spectra of $b = 60$ nm radius system-input parameters: curve 1, $a = 60$ nm, $f_m = 0.0093$, $d_2 = 1.0$ μm , $d_1 = 28$ μm ; curve 2, $a = 205$ nm, $f_m = 0.024$, $d_2 = 1.288$ μm , $d_1 = 26.71$ μm ; curve 3, $a = 320$ nm, $f_m = 0.0314$, $d_2 = 1.520$ μm , $d_1 = 26.48$ μm . The d_3 layer equals 1 μm in all cases.

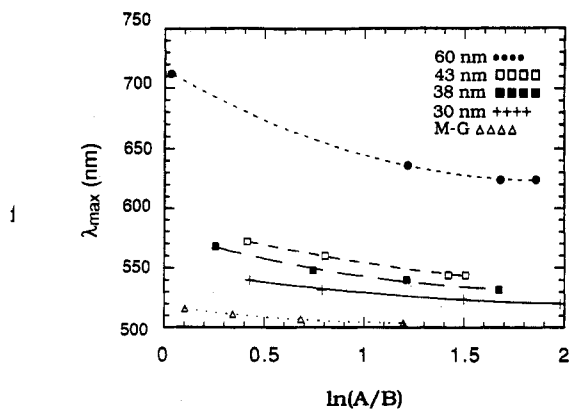


Figure 10. Extinction maxima calculated using M-G theory with size-adjusted depolarization factors q_{eff} plotted against the natural logarithm of the respective particle aspect ratio (A/B). The theoretical points were derived from experimentally determined dimensions, a and b . The curves from top to bottom represent $b = 60, 43, 38$, and 30-nm systems, respectively, with the lowest curve corresponding to the theoretical Maxwell-Garnett limit for infinitely small particles. The lines connecting the data points represent statistical best fit curves.

C. An Approximate Dynamical Maxwell-Garnett Model for Addressing Size and Shape Effects. Mie theory successfully describes size effects but is limited to spheres. In contrast, M-G theory predicts qualitative trends in λ_{max} with shape but cannot deal with size. While there have been numerous scattering

treatments for ellipsoidal^{24a-c} and cylindrical particles,^{25a,b} they are, unfortunately, even more tedious than the Mie treatment for spheres. It is desirable to have a simple, if very approximate, model which deals with size and shape effects simultaneously and is also appropriate for systems in which interparticle separations cannot be considered infinite, as is formally required in single particle scattering treatments such as Mie theory. In this section we propose such a model. The basic strategy is to incorporate a size-dependent depolarization factor into the M-G treatment and then calculate an effective composite dielectric function from which we can simulate spectra.

In 1983, Meier and Wokaun, in an effort to predict metal particle size effects in SERS, derived an alternate expression for the depolarization factor. Specific for spheres, their model defines an effective depolarization factor q_{eff} , which is related to sphere radius a via²⁶

$$q_{\text{eff}} = \frac{1}{3} - \left(\frac{1}{3}\right)k^2 a^2 - \left(\frac{2}{9}\right)ik^3 a^3 \quad (14)$$

where the first term on the right-hand side of eq 14 is the Lorentz depolarizing factor ($q = 1/3$) for spheres. The second term involves *dynamic depolarization* and accounts for the fact that a particle that is not small relative to the incident wavelength will experience different phases of the incident field.²⁷ The term k is equal to $2\pi\tilde{n}_0/\lambda$ (and should not be confused with the absorption coefficient of eqs 4, 7, and 8). The third term accounts for damping of the induced dipole due to radiation emission.²⁷

The expression for spheres in eq 14 was generalized to ellipsoids of revolution by Zeman and Schatz.^{27,28} The dimension of relevance in the size-dependent terms is the ellipsoid axis parallel to the electric field.²⁶⁻²⁹ Therefore, we can calculate an effective screening factor κ_{eff} using

$$q_{\text{eff}} = q_b - \left(\frac{1}{3}\right)k^2 b^2 - \left(\frac{2}{9}\right)ik^3 b^3 \quad (15a)$$

$$\kappa_{\text{eff}} = (1/q_{\text{eff}}) - 1 \quad (15b)$$

where q_b is the depolarization factor for infinitely small particles and b is the semiminor axis of the particles. The choice of b follows from the orientation of our particles in the optical experiments (see Figure 2).

Using the same approach as in section VB but with κ_{eff} replacing κ in eq 6, we calculated spectra for different nanoparticle radii and aspect ratios. Figure 9, B and D, shows these calculated spectra for the 30 and 60 nm particle radius cases, respectively. In each case, as the particle aspect ratio increases, λ_{max} shifts to shorter wavelengths. Also, as seen clearly in the experimental results, Figures 5A,B and 9A,C (both sets of figures are based on identical experimental spectra but are presented with different abscissa limits), the extinction bands for the 60-nm set is red-shifted relative to the 30 nm radius case, and the bands are significantly broadened (again, in accord with experiment). Figure 10 summarizes the calculated λ_{max} values as a function of aspect ratio. The general similarity to Figure 6 is quite apparent, particularly with regard to the degree to which the different pore radius systems are sensitive to shape. For example, the experimental λ_{max} values for the smallest particle systems (30 nm radius) shift about 20 nm going from spherical ($A/B = 1$) to needlelike ($A/B \rightarrow \infty$) geometry. On the other hand, the largest systems (60 nm radius) blue-shift ca. 70 nm going from spherical to needlelike shapes. The analogous shifts based on the dynamical M-G calculation are 48 nm for the 30 nm radius set and 132 nm for the 60-nm systems.

The dynamical M-G approach overestimates λ_{max} in all cases and most seriously at the largest particle radius (for the spherical case, see Table 2). This is not terribly surprising, since we know from the Mie calculations that 60 nm radius spheres scatter considerably. Indeed, what we are attempting to do in the dynamical M-G model is to fold scattering losses into the composite absorption coefficient, k_c . For three of the particle size regimes examined in this study, this approach is certainly not quantitatively correct. However, it does offer simplicity and a reasonable description of trends in λ_{max} , band shape and band intensity.

VI. Conclusions

We have used aluminum anodization and the template synthesis method to prepare nanoscopic gold particles of various radii and aspect ratios. Optical spectra for the gold/alumina composites containing spherical gold particles are quantitatively amenable to Mie theory. The spectra of the higher aspect ratio particle composites show both a size and shape dependence, the latter following qualitatively the predictions of Maxwell-Garnett theory. We propose a simple modification of the M-G treatment using dynamical models for the depolarization factor q developed for SERS theory²⁶⁻²⁹ to deal with size and shape effects in a unified calculation. While this dynamical M-G approach overestimates

λ_{max} , it does capture qualitative trends in λ_{max} , as well as band shape and intensity as the size and shape of the metal particles is varied.

Acknowledgment. We acknowledge Dr. Robert E. Lee and Dr. John Chandler, Colorado State University Electron Microscopy Center; Dr. Keith Carron, University of Wyoming, for useful discussions; Paula J. Davison, electron microscopy support; Ralph S. Schneebeli, Kodak Colorado Division, Windsor; and funding provided by the Office of Naval Research.

References and Notes

- (1) (a) Preston, C. K.; Moskovits, M. *J. Phys. Chem.* **1993**, *97*, 8405. (b) Linnert, T.; Mulvaney, P.; Henglein, A. *J. Phys. Chem.* **1993**, *97*, 679.
- (c) Preston, C. K.; Moskovits, M. *J. Phys. Chem.* **1988**, *92*, 2957.
- (2) (a) Mie, G. *Ann Phys.* **1908**, *25*, 377. (b) van de Hulst, H. C. *Light Scattering by Small Particles*; Dover: New York, 1981.
- (3) (a) Chang, R. K.; Furtak, T. E., Eds. *Surface Enhanced Raman Scattering*; Plenum Press: New York, 1981. (b) Moskovits, M. *Rev. Mod. Phys.* **1985**, *57*, 3, 783.
- (4) (a) Heller, A.; Aspnes, D. E.; Porter, J. D.; Sheng, T. T.; Vadimsky, R. G. *J. Phys. Chem.* **1985**, *89*, 4444. (b) Franzke, D.; Wokaun, A. *J. Phys. Chem.* **1992**, *96*, 6377.
- (5) Goad, D. G. W.; Moskovits, M. *J. Appl. Phys.* **1978**, *49*, 5, 2929.
- (6) (a) Andersson, A.; Hunderi, O.; Granqvist, C. G. *J. Appl. Phys.* **1980**, *51*, 754. (b) Niklasson, G. A. *Solar Energy Materials* **1988**, *17*, 217.
- (7) Liao, P. F. In ref 3a.
- (8) Cai, Z.; Lei, J.; Liang, W.; Menon, V.; Martin, C. R. *Chem. Mater.* **1991**, *3*, 960.
- (9) (a) Tierney, M. J.; Martin, C. R. *J. Phys. Chem.* **1989**, *93*, 2878. (b) Foss, C. A., Jr.; Tierney, M. J.; Martin, C. R. *J. Phys. Chem.* **1992**, *96*, 9001.
- (10) Foss, C. A., Jr.; Hornyak, G. L.; Stockert, J. A.; Martin, C. R. *J. Phys. Chem.* **1992**, *96*, 7497.
- (11) (a) Maxwell-Garnett, J. C. *Philos. Trans. R. Soc. London* **1904**, *302*, 385. (b) Aspnes, D. E. *Thin Solid Films* **1982**, *89*, 249.
- (12) Lide, D. R., Ed. *Handbook of Chemistry and Physics*, 71st ed.; Chemical Rubber Co.: Boca Raton, FL, 1990.
- (13) Abeles, F. In *Advanced Optical Techniques*; Van Heel, A. C. S., Ed.; North Holland: Amsterdam, 1967.
- (14) Equation 8 does not address multiple reflections and thus cannot model interference fringes. Since we do not observe fringes except at the longest wavelengths in the near-IR, eq 8 is appropriate for the present discussion.
- (15) (a) Despic, A.; Parkhutik, V. P. In *Modern Aspects of Electrochemistry*; Bockris, J. O'M., Ed.; Plenum Press: New York 1989, Vol. 20, Chapter 6. (b) Thompson, G. E.; Xu, Y.; Sheldon, P.; Shimizu, K.; Han, S. H.; Wood, G. C. *Philos. Mag. B* **1987**, *55*, 651. (c) Diggle, J. W.; Downie, T. C.; Goulding, C. W. *Chem. Rev.* **1969**, *69*, 365.
- (16) Furneaux, R. C.; Rigby, W. R.; Davidson, A. P. U.S. Patent No. 4,687,551, August 18, 1987.
- (17) While the y-axis is labeled "Absorbance" it should be clear that we are dealing with total extinction which is the sum of particle scattering and absorption losses.
- (18) Johnson, P. B.; Christy, R. W. *Phys. Rev. B* **1972**, *6*, 4370.
- (19) Harns, L. *J. Opt. Soc. Am.* **1955**, *45*, 27.
- (20) For a visual description of the induced moments in spherical particles corresponding to $n = 1, 2, 3$, and 4, see: Born, M.; Wolf, E. *Principles of Optics*, 3rd ed.; Pergamon Press: Oxford, U.K., 1965.
- (21) See ref 2b and: Aspnes, et al. *J. Appl. Phys.* **1986**, *60*, 3028.
- (22) We determined n_0 by plotting $\ln(T_{\text{tot}})$ versus d for four anodic aluminum oxide films grown to different thicknesses. From eq 8, we obtain k_0 from the slope and n_0 from the y-intercept. Since these films are porous, a back-calculation using the M-G equation applied to an alumina/air composite yielded the optical constants for the pure oxide. The refractive index for the pure oxide was found to be ca. 1.5–1.6 for most of the visible and near-IR spectrum.
- (23) Kittel, C. *Solid State Physics*, 6th ed.; John Wiley and Sons: New York, 1986.
- (24) (a) Molt, A. R.; Uzunoglu, N. K.; Evans, B. G. *IEEE Trans. Antennas Propagat.* **1978**, *AP-6*, 706. (b) Asano, S.; Yamamoto, G. *Appl. Opt.* **1975**, *14*, 29. (c) Stevenson, A. F. *J. Appl. Phys.* **1953**, *24*, 1143.
- (25) (a) Ruppin, R. *J. Phys. D: Appl. Phys.* **1990**, *23*, 757. (b) Swathi, P. S.; Tong, T. W. *J. Quant. Spectrosc. Radiat. Transfer* **1988**, *40*, 525.
- (26) Meier, M.; Wokaun, A. *Optics Lett.* **1983**, *8*, 581.
- (27) Zeman, E. J.; Schatz, G. C. In *Proceedings of the 17th Jerusalem Symposium*; Pullman, B., Hortner, J., Nitzan, A., Gerber, B., Eds.; Reidel: Dordrecht, Holland, 1984; p 413.
- (28) Zeman, E. J.; Schatz, G. C. *J. Phys. Chem.* **1987**, *91*, 634.
- (29) Carron, K., manuscript in preparation.